

Direct observation of layer skyrmions in twisted WSe₂ bilayers

Fan Zhang^{1†}, Nicolás Morales-Durán^{1†}, Yanxing Li^{1†}, Wang Yao², Jung-Jung Su³, Yu-Chuan Lin^{4,5}, Chengye Dong⁴, Hyunsue Kim¹, Joshua A. Robinson⁴, Allan H. Macdonald^{1*}, and Chih-Kang Shih^{1*}

¹Department of Physics, University of Texas at Austin, Austin, TX, USA

²Department of Physics, The University of Hong Kong, Hong Kong, China

³Department of Electrophysics, National Yang Ming Chiao Tung University, Hsinchu, Taiwan

⁴Department of Materials Science and Engineering, Pennsylvania State University, University Park, PA, USA

⁵Department of Materials Science and Engineering, National Yang Ming Chiao Tung University, Hsinchu, Taiwan

[†]These authors contribute equally to this work.

*Corresponding authors' email: macdpc@physics.utexas.edu; shih@physics.utexas.edu

Abstract

Transition metal dichalcogenide (TMD) twisted homobilayers have been established as an ideal platform for studying strong correlation phenomena, as exemplified by the recent discovery of fractional Chern insulator (FCI) states in twisted MoTe₂¹⁻⁴ and Chern insulators (CI)⁵ and unconventional superconductivity^{6,7} in twisted WSe₂. In these systems, nontrivial topology in the strongly layer-hybridized regime can arise from a spatial patterning of interlayer tunneling amplitudes and layer-dependent potentials that yields a lattice of layer skyrmions. Here we report the direct observation of skyrmion textures in the layer degree of freedom of Rhombohedral-stacked (R-stacked) twisted WSe₂ homobilayers. This observation is based on scanning tunneling spectroscopy that separately resolves the Γ -valley and K-valley moiré electronic states. We show that Γ -valley states are subjected to a moiré potential with an amplitude of ~ 120 meV. At ~ 150 meV above the Γ -valley, the K-valley states are subjected to a weaker moiré potential of ~ 30 meV. Most significantly, we reveal opposite layer polarization of the K-valley at the MX and XM sites within the moiré unit cell, confirming the theoretically predicted skyrmion layer-texture. The dI/dV mappings allow the parameters that enter the continuum model for the description of moiré bands in twisted TMD bilayers to be determined experimentally, further establishing a direct correlation between the shape of LDOS profile in real space and topology of topmost moiré band.

Main

Semiconducting transition metal dichalcogenide (TMD) moiré materials have attracted significant attention within the last few years, as they offer a tunable platform to study quantum phenomena arising from correlation and topology⁸⁻¹⁵. In particular, some R-stacked twisted homobilayers in which the top of the spin-valley locked valence band comes from the K (-K)-valley, like MoTe₂ and WSe₂, provide an opportunity to explore the realm of topologically-ordered states^{13,16-30}, as experimentally confirmed with the observation of the fractional quantum anomalous Hall effect (FQAHE)²⁻⁴ and the fractional quantum spin Hall effect (FQSHE)³¹. Continuum-model theoretical descriptions of R-stacked homobilayers include a local layer-dependent term that contains one layer skyrmion per moiré unit cell^{10,32,33}. Subsequent studies have shown that this skyrmion structure plays a crucial role in determining the topological character of the band^{10,32-34}, giving rise to a real-space Berry curvature of quantized flux per moiré unit cell. With the capability of probing atomic structure and local electronic properties, scanning tunneling microscopy (STM) is an ideal tool to investigate this unique skyrmion-like layer pseudospin. However, it requires the ability to separate Γ -valley and K-valley state, which is non-trivial due to the valley dependent tunneling decay coefficient.

In this work we perform STM/S measurements to directly probe the opposite layer polarizations at MX and XM positions, thereby revealing the layer-skyrmion texture in an R-stacked WSe₂ bilayer twisted to 5.1 degrees, in agreement with theoretical modeling. Following previously developed methodology^{35,36}, Γ - and K-valley states are resolved individually by combining conventional STS, which is more sensitive to the Γ -valley states, with constant current STS, which greatly enhances the sensitivity to the K-valley states. This capability allows us to reveal the moiré potential modulations for Γ -valley and K-valley separately. In addition, the layer skyrmion texture is manifested by opposite polarizations of the K-valley wavefunction between the MX and XM sites. This direct experimental observation of the pseudospin texture and the moiré potential modulation sheds light on the parameters of the continuum model theoretical description^{10,37}, which is key to experimental searches for exotic topological phases (e.g. FQAHE) in twisted TMD systems. This unique feedback loop may deepen the understanding of the conditions required for

the emergence of Chern bands and promote the discovery of exotic new topological phases in moiré TMDs.

Theoretical modeling of twisted TMD homobilayers

We first discuss the continuum model description of the K-valleys in twisted TMD homobilayers, from which the layer pseudospin picture emerges. At a small twist angle θ , a moiré superlattice with a lattice constant $a_M \sim 10$ nm will be created as shown in Fig. 1a. Top view and side view of the bilayer structure for three high symmetry configurations (marked as AA, MX, XM) are shown in Fig. 1b. At the MX site, the transition metal (M) of the top layer is aligned with the chalcogen atom (X) of the bottom layer. While at XM site, the chalcogen atom (X) of the top layer is aligned with the transition metal (M) of the bottom layer. The AA site corresponds to the stacking at which the transition metal atoms from both layers are aligned. Figure 1c shows the moiré Brillouin zone (MBZ) emerging from the relative twist between top and bottom layer BZ. The K points from the top layer (\mathbf{K}_t) and bottom layer (\mathbf{K}_b) are located at adjacent MBZ corners, as illustrated in Fig. 1c. Due to spin-valley locking³⁸, the topmost valence bands in K and $-\mathbf{K}$ valleys have opposite spin orientation (up for K, down for $-\mathbf{K}$). Because the K and $-\mathbf{K}$ valleys are related by time-reversal symmetry, we can focus on the Hamiltonian for the K valley, written in layer space as

$$H_K = \begin{pmatrix} -\frac{\hbar^2(\mathbf{k} - \mathbf{K}_b)^2}{2m^*} + \Delta_b(\mathbf{r}) & \Delta_T(\mathbf{r}) \\ \Delta_T^\dagger(\mathbf{r}) & -\frac{\hbar^2(\mathbf{k} - \mathbf{K}_t)^2}{2m^*} + \Delta_t(\mathbf{r}) \end{pmatrix}.$$

After applying a unitary transformation, $U_0 = \text{diag}(e^{i\mathbf{K}_b \cdot \mathbf{r}}, e^{i\mathbf{K}_t \cdot \mathbf{r}})$, to remove the momentum shifts in the diagonal, the Hamiltonian is given by

$$H_K = -\frac{\hbar^2 \mathbf{k}^2}{2m^*} \sigma_0 + \mathbf{\Delta}(\mathbf{r}) \cdot \boldsymbol{\sigma} + \Delta_0 \sigma_0,$$

where $\boldsymbol{\sigma} = (\sigma_x, \sigma_y, \sigma_z)$ are the layer Pauli matrices and σ_0 is the identity. The layer-dependent moiré potentials and the interlayer tunneling are respectively given by

$$\Delta_{b/t}(\mathbf{r}) = \sum_{j=1,3,5} 2V_m \cos(\mathbf{b}_j \cdot \mathbf{r} \pm \psi),$$

$$\Delta_T(\mathbf{r}) = \omega(e^{iq_1 \cdot \mathbf{r}} + e^{iq_2 \cdot \mathbf{r}} + e^{iq_3 \cdot \mathbf{r}}),$$

With $\mathbf{q}_1 = \mathbf{K}_b - \mathbf{K}_t$, $\mathbf{q}_2 = \mathbf{b}_2 + \mathbf{q}_1$, $\mathbf{q}_3 = \mathbf{b}_3 + \mathbf{q}_1$, where the \mathbf{b}_j belong to the first shell of reciprocal lattice vectors. We have defined $\mathbf{\Delta}(\mathbf{r}) = (Re\Delta_T, Im\Delta_T, (\Delta_b - \Delta_t)/2)$ and $\Delta_0 = (\Delta_b + \Delta_t)/2$. When the layer degree of freedom is understood as a pseudospin, the continuum model Hamiltonian corresponds to a fermion in the presence of an effective Zeeman field $\mathbf{\Delta}$ acting on the layer pseudospin, whose spatial structure is shown in Fig. 1d. This layer-Zeeman field forms a texture with one skyrmion per moiré unit cell, with its bottom component vanishing at the XM site and its top component vanishing at the MX site. If the layer-pseudospin of holes aligns with the direction of $\mathbf{\Delta}$, the corresponding wave functions will acquire a winding as they cover the moiré unit cell, resulting in a real space Berry curvature that plays the role of an effective magnetic field with quantized flux per moiré cell²⁸.

It has been suggested that the particular spatial form of the layer pseudospin in TMD homobilayers is crucial for the emergence of non-zero Chern numbers in the moiré mini bands. This new perspective to understand the physics of TMD homobilayers could provide new insights into the nature of the topologically-ordered states that have been observed in these systems. However, up to this point there is no direct experimental evidence to confirm that the layer pseudospin state ranges over its full Bloch sphere, with opposite full layer polarizations (layer-pseudospin) at the XM and MX sites, arising from alignment between layer pseudospins and layer-skyrmion fields.

The presence of the skyrmion texture in the layer-pseudospin degree of freedom does not guarantee the emergence of topological bands. The tunneling and moiré potentials in the continuum model depend on three material-specific parameters (V_m, ψ, ω), (V_m : moiré potential amplitude, ψ : moiré potential phase, ω : interlayer hopping) and the Chern number of the topmost moiré mini band depends crucially on the interplay of these parameters. The usual approach to estimate the continuum model parameters is via large-scale ab initio structure calculations that have all the uncertainties of DFT theory. Here we show that local probe measurements provide a route to extract values directly from the experiment.

STM observation of layer-pseudospin skyrmions

We now discuss our experimental observation of layer-pseudospin textures. Figure 2a shows the schematic STM experimental measurement set-up of a small angle twisted WSe₂ homobilayer.

The sample was grown on a graphene substrate with metal organic chemical vapor deposition (MOCVD) with small angle twisted homobilayer regions (See in Supplementary Information, Fig. S1 and S2). Shown in Fig. 2b is an STM image of a moiré superlattice with a wavelength $a_M = 3.71\text{nm}$. From the measured value of a_M the twist angle $\theta = 5.1^\circ$ can be extracted through $a_M = a/(2 \sin(\frac{\theta}{2}))$, where the WSe₂ monolayer lattice constant a is 0.328nm . Shown in Fig. 2c are tunneling spectra acquired at four sites marked as AA, MX, Bridge (Br), XM in Fig. 2b. Here the spectra are acquired using the conventional STS mode where the tip-to-sample distance is maintained at a constant value while the sample bias is varied (referred to as a constant height STS or CH-STS). As shown in Fig. 2c, the energy of the topmost Γ band is lower at the AA sites than that at the MX/XM sites by an amount of ~ 120 meV, corresponding to a moiré potential modulation amplitude of 120 meV. This results from the higher interlayer spacing at the AA sites, which lowers the hybridization strength. This value for the Γ - moiré modulations agrees well with recent reports^{39,40}. However, electronic states modulations near the K points were not reported. This is because states near the K-point decay very rapidly into the vacuum as discussed previously by Zhang et al³⁵. A direct measurement of the decay constant for Γ - and K-valley states is shown in Supplementary Fig. S3. At a typical tip-to-sample distance of 10 \AA , the tunneling probability of K-valley states is several orders of magnitude smaller than the Γ -valley states. This low sensitivity can be overcome by taking STS in the constant current mode (referred to as CC-STS) which automatically brings the tip-to-sample distance closer when only states in the K-valley are available for tunneling as depicted in Supplementary Fig. S4. Shown in Fig. 2d are the spectra acquired using the CC-STS mode which uncovers a K valley modulation of around 30 meV, much smaller compared with the Γ -valley states, due to the weak interlayer hybridization of the K-valley states. More significantly, at the K valley, the spectrum acquired at the XM site is of higher intensity than that at the MX site, due to layer-polarized K-valley wavefunctions (layer pseudospin) resulting from a combination of weak interlayer hybridization and the effective electric field arising from interlayer charge transfer^{41,42}.

Shown in Fig. 3a is the colormap of CH-STS spectra along high-symmetry directions of the moiré superlattice [AA-MX-Br-XM-AA]. The energy difference of the topmost Γ bands, between AA site and MX/XM sites reflects the large moiré potential modulation amplitude ~ 0.12 eV of the Γ

valley. The color map of CC-STs shows that the K-valley states are located about 0.15 eV above the Γ valley, with a weaker (~ 30 meV) variation in peak position (Fig. 3b). Crucially, the intensity exhibits a striking contrast, especially between MX and XM sites. At the MX site, the W atom in the top layer is aligned with the Se atoms at the bottom layer, and vice-versa for the XM site. This results in opposite interlayer polarizations with a dipole pointing down at the MX site and up at the XM site, leading to opposite wavefunction localization at the top (XM) and bottom (MX) layers.

We next investigate the 2D texture of the K valley (see 2D texture of the Γ valley in Supplementary Fig. S5). Shown in Fig. 3c is the STM topography acquired at -0.85V. This bias corresponds to the black dashed line shown in Fig. 3b where the tunneling primarily results from electronic states at the K valley. Shown in Fig. 3d is the conductivity image acquired at -0.85 V, at a constant height, and with a lock-in modulation amplitude of 20 mV. The modulation bandwidth is large enough to cover most of the states near the VBM and the image can be viewed as capturing the spatial modulation of the local density of states near the VBM. Acquiring the conductivity image at a constant height also removes the uncertainty associated with a varying tip-to-sample distance in the topography image (Also see the constant current conductivity image in Supplementary Fig. S6). In this conductivity image atomic lattice corrugations are also observed which can be removed by filtering out the Bragg peak in the FFT (shown as Fig. 3e). Note that the local density-of-states (DOS) at the XM and MX sites are identical. Thus, the intensity difference reflects a layer polarization difference and can be used to represent the texture of the layer pseudospins. (The same argument does not apply to the K-valley states at other sites (AA and Br) since the local DOS also varies with position.) Regardless, the contrast between the MX and XM sites reflects the skyrmion texture of the layer pseudospin degree of freedom.

To better capture the pseudospin texture, we interpret the STM results by comparing with theoretical simulations using parameterized continuum models.

Continuum model parameters from STS

We interpret the dI/dV map shown Fig. 3e as a layer-projected LDOS. We compare the spatial profile along AA-MX-Br-XM-AA, shown as the black solid curve in Fig. 4a, with the local maximum of the theoretical LDOS near K_{VBM}

$$D(\mathbf{r}, \varepsilon) = \mathcal{N} \sum_{\mathbf{k}} |\psi_{\mathbf{k}}^t(\mathbf{r})|^2 \exp\left(-\frac{(\varepsilon - \varepsilon_{\mathbf{k}})^2}{2\sigma^2}\right),$$

calculated using the continuum model and adjusting parameters to match experiment. Here $\psi_{\mathbf{k}}^t(\mathbf{r})$ is the top-layer component of the continuum model eigenstate, $\varepsilon_{\mathbf{k}}$ is a continuum model energy and \mathcal{N} is a normalization constant. Here we have assumed a Gaussian resolution window for our scanning probe tip with a width σ of around 20 meV. The best theoretical fit is plotted as red dashed line in Fig. 4a. From this fit we estimate the continuum model parameters for 5.08° twisted WSe₂ to be $V_m = 34.8$ meV, $\psi = 42.1$ degrees and $\omega = 7.2$ meV. (We also take the effective mass of carriers as a fitting parameter and obtain $m = 0.4m_0$.) Figure 4b shows the moiré band structure corresponding to these parameters, which displays a topmost mini band with ~ 70 meV bandwidth. The Chern number of the topmost band is zero, indicating a topologically trivial topmost band. These parameters lead to the pseudospin texture shown in Fig. 4c. The false color rendition represents the z-component of the layer pseudospin while the in-plane component is labeled by the black arrows. By this route, scanning tunneling microscopy techniques can be used to reveal the topological character of moiré TMD samples. The sensitivity of the continuum model fit to the experimental data is illustrated in Fig. 4d, where we plot the layer-projected LDOS as a function of position for two different sets of parameters. The green dashed curve with $V_m = 34.8$ meV, $\psi = 42.1$ degrees, and $\omega = 21.6$ meV still agrees reasonably well with the experiment even though ω has been increased substantially. The blue dashed curve with $V_m = 34.8$ meV, $\psi = 150$ degrees, and $\omega = 7.2$ meV, has a completely different shape. Figure 4e shows the Chern number of the topmost moiré band from the continuum model as a function of ψ and V_m/ω at $\theta=5.08^\circ$. The two sets of parameters from Figure 4d lead to topmost bands with $C=0$ and $C=1$ respectively and they are labeled in the parameter space as the green and blue stars. Also shown as a red star corresponds to the parameters used in the earlier fit in Fig. 4a. As can be seen, the fit is most sensitive to the parameter ψ , which is also the parameter that is most crucial in interpreting the band topology as emphasized in Fig. 4e. This comparison also establishes a very important correlation between the LDOS profile, an observable using STS, and the quantum geometry that determines the band topology.

We note that an independent STM/S investigation of a 2.75° twisted MoTe₂ bilayer system⁴³, a known Chern insulator¹⁻⁴, showed a very similar Γ -valley moiré potential and a similar pseudospin

texture for the K-valley. However, in that work it was reported that the lowest energy hole states are residing at the MX/XM sites and a topologically non-trivial topmost band. Considering that the Chern number distribution in continuum model parameter space for twisted MoTe₂ is similar to the WSe₂ case, this result is actually close to the blue dashed line in Fig. 4d corresponding to non-zero Chern number, providing another good evidence that K-valley density of state mapping can be used to determine the moiré band topology. In this regard, these two independent investigations corroborate very well with each other.

It is important to point out that at a twist angle smaller than 3°, strong atomic reconstruction occurs^{41,44-46}, leading to the maximization of MX/XM domains with sharp domain walls and minimization of AA region, and a strong strain effect is expected. On the other hand, at 5° twist, such reconstruction does not happen, and the MX/XM domains are smaller. Yet, the layer pseudospin skyrmions remain observable.

Summary and Discussion

In summary, we performed scanning tunneling microscopy/spectroscopy (STM/STS) to probe the local electronic states of small angle twisted WSe₂, providing evidence for the presence of skyrmion in the layer degree of freedom. We show that STS provides very valuable local electronic information about moiré TMD homobilayers, which is complementary to what can be extracted from current optical and transport measurements. Topological bands have been probed in smaller twist angle WSe₂ and Chern insulator states were experimentally revealed⁵, but a complete understanding of the requirements for Chern bands to emerge in these materials is still lacking. To tackle this issue, we introduced a method of obtaining the theoretical continuum model parameters which further determine the existence of Chern bands by fitting the LDOS revealed by STS. More significantly, we establish a direct correlation between the shape of LDOS profile in real space and the Chern number. In terms of designing strong correlated states e.g. FCI from first principles, our method could be a good alternative to DFT calculations, because DFT calculations are unlikely to be sufficiently accurate due to challenges including non-local exchange interactions. Our method is applicable to all material systems that can be probed by STM, and will play a pivotal role in sorting out the interaction physics of many fundamentally interesting states.

Methods

Sample growth for STM

High-quality buffer on SiC was synthesized using a two-step process. First, the monolayer epitaxial graphene was synthesized using silicon sublimation from the Si face of the semi-insulating SiC substrates (II–VI). Before the growth, the SiC substrates were annealed in 10% hydrogen (balance argon) at 1,500 °C for 30 min to remove subsurface damages due to chemical and mechanical polishing. Then monolayer epitaxial graphene (MLEG) was formed at 1,800 °C for 30 min in a pure argon atmosphere. Second, an Ni stressor layer was used to exfoliate the top graphene layer to obtain fresh and high-quality buffer on SiC. After this, 270 nm of Ni was e-beam deposited on MLEG at a rate of 5 \AA s^{-1} as a stressor layer. Then a thermal release tape was used to peel off the top graphene layer from the substrate. The growth of WSe₂ crystals on an epitaxial graphene substrate was carried out at 800 °C in a custom-built vertical cold-wall chemical vapor deposition (CVD) reactor for 20 min⁴⁷. The tungsten hexacarbonyl (W(CO)₆) (99.99%, Sigma-Aldrich) source was kept inside a stainless-steel bubbler in which the temperature and pressure of the bubbler were always held at 37 °C and 730 torr, respectively. Mass-flow controllers were used to supply H₂ carrier gas to the bubbler to transport the W(CO)₆ precursor into the CVD chamber. The flow rate of the H₂ gas through the bubbler was maintained at a constant 8 standard cubic centimeters per minute (sccm), which resulted in a W(CO)₆ flow rate of 9.0×10^{-4} sccm at the outlet of the bubbler. H₂Se (99.99%, Matheson) gas was supplied from a separate gas manifold and introduced at the inlet of the reactor at a constant flow rate of 30 sccm.

STM and STS measurements

STM and STS measurements were conducted at 4.3 K in the ultra-high vacuum chamber, with a base pressure of 2.0×10^{-11} torr. The W tip was prepared by electrochemical etching and then cleaned by in situ electron-beam heating. STM dI/dV spectra were measured using a standard lock-in technique, for which the modulation frequency was 758 Hz. Two different modes of STS were simultaneously used: (1) the conventional constant-height STS and (2) the constant-current STS.

Acknowledgement

Y.L., F.Z., H.K. and C.-K.S. were supported by the NSF through the Center for Dynamics and Control of Materials: an NSF Materials Research Science and Engineering Center under cooperative agreement no. DMR-2308817, the US Air Force grant no. FA2386-21-1-4061, NSF grant nos. DMR-1808751 and DMR-2219610, and the Welch Foundation F-2164. N.M.D and A.H.M were supported by the U.S. Department of Energy Office of Basic Energy Sciences under Award DE-SC0019481. C. D. and J. A. R. were supported by the Penn State Center for Nanoscale Science (NSF grant no. DMR-2011839) and the Penn State 2DCC-MIP (NSF grant no. DMR-1539916). Y.-C.L. acknowledges the support from the Center for Emergent Functional Matter Science (CEFMS) of NYCU and the Yushan Young Scholar Program from the Ministry of Education of Taiwan.

Author Contributions

F.Z. and Y.L. carried out the STM and STS measurements under the supervision of C.-K.S. N.M.D performed the theoretical modeling under the supervision of A. H. M. Y.-C.L. synthesized the twisted WSe₂ bilayers. C.D. prepared the graphitic buffer layer/SiC. J.A.R. supervised the sample preparation. H.K. annealed and pre-treated the sample. Y.L., F.Z., and C.-K.S. analyzed the STM data. W. Y. and Jung-Jung Su involved in the discussion of layer pseudospin. F.Z., N.M.D, Y.L., A. H. M. and C.-K.S. wrote the paper with contributions from all the authors. † These authors contributed equally to this work.

Competing Interests: All the authors declare no competing interests.

Data Availability: Source data that reproduces the plots in the main text are provided with this paper. All other data that support the findings of this study are available from the corresponding author upon request.

References

1. Cai, J. *et al.* Signatures of fractional quantum anomalous Hall states in twisted MoTe₂. *Nature* **622**, 63–68 (2023).
2. Park, H. *et al.* Observation of fractionally quantized anomalous Hall effect. *Nature* **622**, 74–79 (2023).
3. Zeng, Y. *et al.* Thermodynamic evidence of fractional Chern insulator in moiré MoTe₂. *Nature* **622**, 69–73 (2023).
4. Xu, F. *et al.* Observation of Integer and Fractional Quantum Anomalous Hall Effects in Twisted Bilayer MoTe₂. *Phys. Rev. X* **13**, 031037 (2023).
5. Foutty, B. A. *et al.* Mapping twist-tuned multiband topology in bilayer WSe₂. *Science* **384**, 343–347 (2024).
6. Guo, Y. *et al.* Superconductivity in twisted bilayer WSe₂. Preprint at <http://arxiv.org/abs/2406.03418> (2024).
7. Xia, Y. *et al.* Unconventional superconductivity in twisted bilayer WSe₂. *ArXiv Prepr. ArXiv240514784* (2024).
8. Andrei, E. Y. *et al.* The marvels of moiré materials. *Nat. Rev. Mater.* **6**, 201–206 (2021).
9. Angeli, M. & MacDonald, A. H. Γ valley transition metal dichalcogenide moiré bands. *Proc. Natl. Acad. Sci.* **118**, e2021826118 (2021).
10. Wu, F., Lovorn, T., Tutuc, E., Martin, I. & MacDonald, A. H. Topological Insulators in Twisted Transition Metal Dichalcogenide Homobilayers. *Phys. Rev. Lett.* **122**, 086402 (2019).
11. Xu, Y. *et al.* A tunable bilayer Hubbard model in twisted WSe₂. *Nat. Nanotechnol.* **17**, 934–939 (2022).
12. Pan, H., Wu, F. & Das Sarma, S. Band topology, Hubbard model, Heisenberg model, and Dzyaloshinskii-Moriya interaction in twisted bilayer WSe₂. *Phys. Rev. Res.* **2**, 033087 (2020).
13. Dong, J., Wang, J., Ledwith, P. J., Vishwanath, A. & Parker, D. E. Composite Fermi Liquid at Zero Magnetic Field in Twisted MoTe₂. *Phys. Rev. Lett.* **131**, 136502 (2023).
14. Li, H. *et al.* Contrasting twisted bilayer graphene and transition metal dichalcogenides for fractional Chern insulators: an emergent gauge picture. Preprint at <http://arxiv.org/abs/2402.02251> (2024).

15. Zhang, Y., Liu, T. & Fu, L. Electronic structures, charge transfer, and charge order in twisted transition metal dichalcogenide bilayers. *Phys. Rev. B* **103**, 155142 (2021).
16. Devakul, T., Crépel, V., Zhang, Y. & Fu, L. Magic in twisted transition metal dichalcogenide bilayers. *Nat. Commun.* **12**, 6730 (2021).
17. Bi, Z. & Fu, L. Excitonic density wave and spin-valley superfluid in bilayer transition metal dichalcogenide. *Nat. Commun.* **12**, 642 (2021).
18. Wang, L. *et al.* Correlated electronic phases in twisted bilayer transition metal dichalcogenides. *Nat. Mater.* **19**, 861–866 (2020).
19. Ghiotto, A. *et al.* Quantum criticality in twisted transition metal dichalcogenides. *Nature* **597**, 345–349 (2021).
20. Magorrian, S. J. *et al.* Multifaceted moiré superlattice physics in twisted WSe_2 bilayers. *Phys Rev B* **104**, 125440 (2021).
21. Li, H., Kumar, U., Sun, K. & Lin, S.-Z. Spontaneous fractional Chern insulators in transition metal dichalcogenide moiré superlattices. *Phys. Rev. Res.* **3**, L032070 (2021).
22. Kundu, S., Naik, M. H., Krishnamurthy, H. R. & Jain, M. Moiré induced topology and flat bands in twisted bilayer WSe_2 : A first-principles study. *Phys. Rev. B* **105**, L081108 (2022).
23. Crépel, V. & Fu, L. Anomalous Hall metal and fractional Chern insulator in twisted transition metal dichalcogenides. *Phys. Rev. B* **107**, L201109 (2023).
24. Reddy, A. P., Alsallom, F. F., Zhang, Y., Devakul, T. & Fu, L. Fractional quantum anomalous Hall states in twisted bilayer MoTe_2 and WSe_2 . *Phys. Rev. B* **108**, 085117 (2023).
25. Zhang, X.-W. *et al.* Polarization-driven band topology evolution in twisted MoTe_2 and WSe_2 . *Nat. Commun.* **15**, 4223 (2024).
26. Wang, C. *et al.* Fractional Chern Insulator in Twisted Bilayer MoTe_2 . *Phys. Rev. Lett.* **132**, 036501 (2024).
27. Fan, F.-R., Xiao, C. & Yao, W. Orbital Chern insulator at $\nu = -2$ in twisted MoTe_2 . *Phys. Rev. B* **109**, L041403 (2024).
28. Morales-Durán, N., Shi, J. & MacDonald, A. H. Fractionalized electrons in moiré materials. *Nat. Rev. Phys.* (2024) doi:10.1038/s42254-024-00718-z.
29. Wang, T., Devakul, T., Zaletel, M. P. & Fu, L. Topological magnets and magnons in twisted bilayer MoTe_2 and WSe_2 . Preprint at <http://arxiv.org/abs/2306.02501> (2023).
30. Redekop, E. *et al.* Direct magnetic imaging of fractional Chern insulators in twisted MoTe_2 with a superconducting sensor. Preprint at <http://arxiv.org/abs/2405.10269> (2024).
31. Kang, K. *et al.* Evidence of the fractional quantum spin Hall effect in moiré MoTe_2 . *Nature* **628**, 522–526 (2024).
32. Yu, H., Chen, M. & Yao, W. Giant magnetic field from moiré induced Berry phase in homobilayer semiconductors. *Natl. Sci. Rev.* **7**, 12–20 (2020).
33. Morales-Durán, N., Wei, N., Shi, J. & MacDonald, A. H. Magic Angles and Fractional Chern Insulators in Twisted Homobilayer Transition Metal Dichalcogenides. *Phys. Rev. Lett.* **132**, 096602 (2024).
34. Zhai, D. & Yao, W. Theory of tunable flux lattices in the homobilayer moiré of twisted and uniformly strained transition metal dichalcogenides. *Phys. Rev. Mater.* **4**, 094002 (2020).
35. Zhang, C. *et al.* Probing Critical Point Energies of Transition Metal Dichalcogenides: Surprising Indirect Gap of Single Layer WSe_2 . *Nano Lett.* **15**, 6494–6500 (2015).
36. Li, Y. *et al.* Tuning commensurability in twisted van der Waals bilayers. *Nature* **625**, 494–499 (2024).

37. Wu, F., Lovorn, T., Tutuc, E. & MacDonald, A. H. Hubbard Model Physics in Transition Metal Dichalcogenide Moiré Bands. *Phys. Rev. Lett.* **121**, 026402 (2018).
38. Xu, X., Yao, W., Xiao, D. & Heinz, T. F. Spin and pseudospins in layered transition metal dichalcogenides. *Nat. Phys.* **10**, 343–350 (2014).
39. Pei, D. *et al.* Observation of Γ -Valley Moiré Bands and Emergent Hexagonal Lattice in Twisted Transition Metal Dichalcogenides. *Phys. Rev. X* **12**, 021065 (2022).
40. Gatti, G. *et al.* Flat Γ Moiré Bands in Twisted Bilayer WSe₂. *Phys. Rev. Lett.* **131**, 046401 (2023).
41. Weston, A. *et al.* Atomic reconstruction in twisted bilayers of transition metal dichalcogenides. *Nat. Nanotechnol.* **15**, 592–597 (2020).
42. Wang, X. *et al.* Interfacial ferroelectricity in rhombohedral-stacked bilayer transition metal dichalcogenides. *Nat. Nanotechnol.* **17**, 367–371 (2022).
43. Thompson, E. *et al.* Visualizing the microscopic origins of topology in twisted molybdenum ditelluride. Preprint at <http://arxiv.org/abs/2405.19308> (2024).
44. Weston, A. *et al.* Interfacial ferroelectricity in marginally twisted 2D semiconductors. *Nat. Nanotechnol.* **17**, 390–395 (2022).
45. Ezzi, M. M. A., Pallewela, G. N., De Beule, C., Mele, E. J. & Adam, S. Analytical Model for Atomic Relaxation in Twisted Moiré Materials. Preprint at <http://arxiv.org/abs/2401.00498> (2024).
46. Tilak, N., Li, G., Taniguchi, T., Watanabe, K. & Andrei, E. Y. Moiré Potential, Lattice Relaxation, and Layer Polarization in Marginally Twisted MoS₂ Bilayers. *Nano Lett.* **23**, 73–81 (2023).
47. Lin, Y.-C. *et al.* Realizing Large-Scale, Electronic-Grade Two-Dimensional Semiconductors. *ACS Nano* **12**, 965–975 (2018).

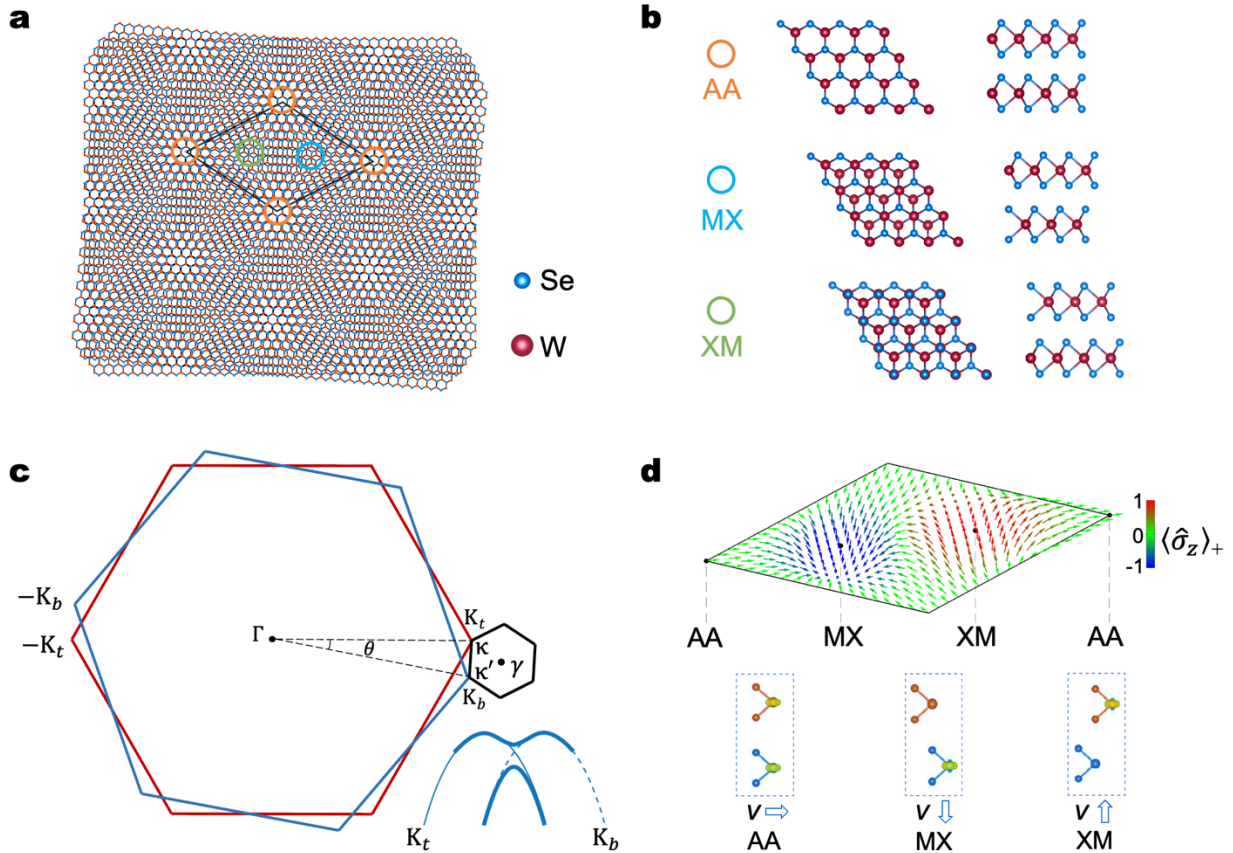


Figure 1 | Moiré superlattice and layer pseudospin. **a**, Schematic of a moiré superlattice in a 5.1-degree twisted WSe₂ homobilayer. The high-symmetry AA, MX and XM sites are respectively marked with orange, blue and green circles. **b**, Top and side views of the structures AA, MX and XM stacking. **c**, Brillouin zones of the top (red) and bottom (blue) layers in a twisted bilayer, and the moiré Brillouin zone (black). Bottom right: schematic of the band hybridization between top and bottom layer K valley valence bands. **d**, Top, Layer pseudospin texture of small angle twisted bilayer WSe₂. The arrows indicate layer pseudospin orientations and the color codes its z component. Bottom, corresponding layer distributions of valence band edge carriers (yellow isosurfaces), at the three high symmetry stackings, with the arrows indicating the layer pseudospin orientations.

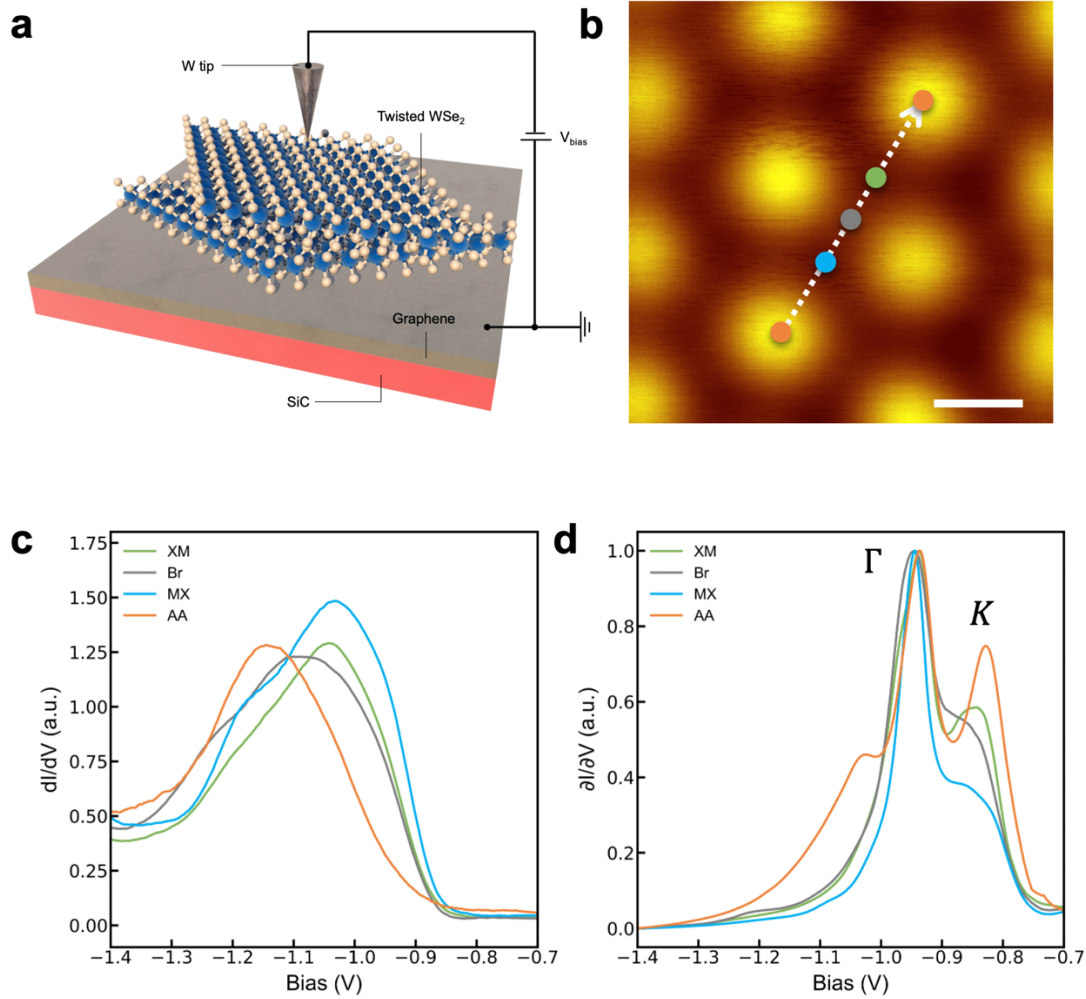


Figure 2 | Γ and K valley moiré modulated tunneling spectroscopies. **a**, STM topography image at ($V = -2$ V, $I = -50$ pA). **b**, STM image showing the moiré pattern with a periodicity of 3.7 nm, which corresponds to a twist angle 5.1 degree. Scale bar: 2 nm. **c**, Constant height STS at four sites: AA, MX, Br, XM. ($V_{\text{int}} = -2.2$ V, $I = -100$ pA and $V_{\text{amp}} = 30$ mV) **d**, Constant current STS at four sites. ($V_{\text{int}} = -1.4$ V, $I = -100$ pA and $V_{\text{amp}} = 20$ mV)

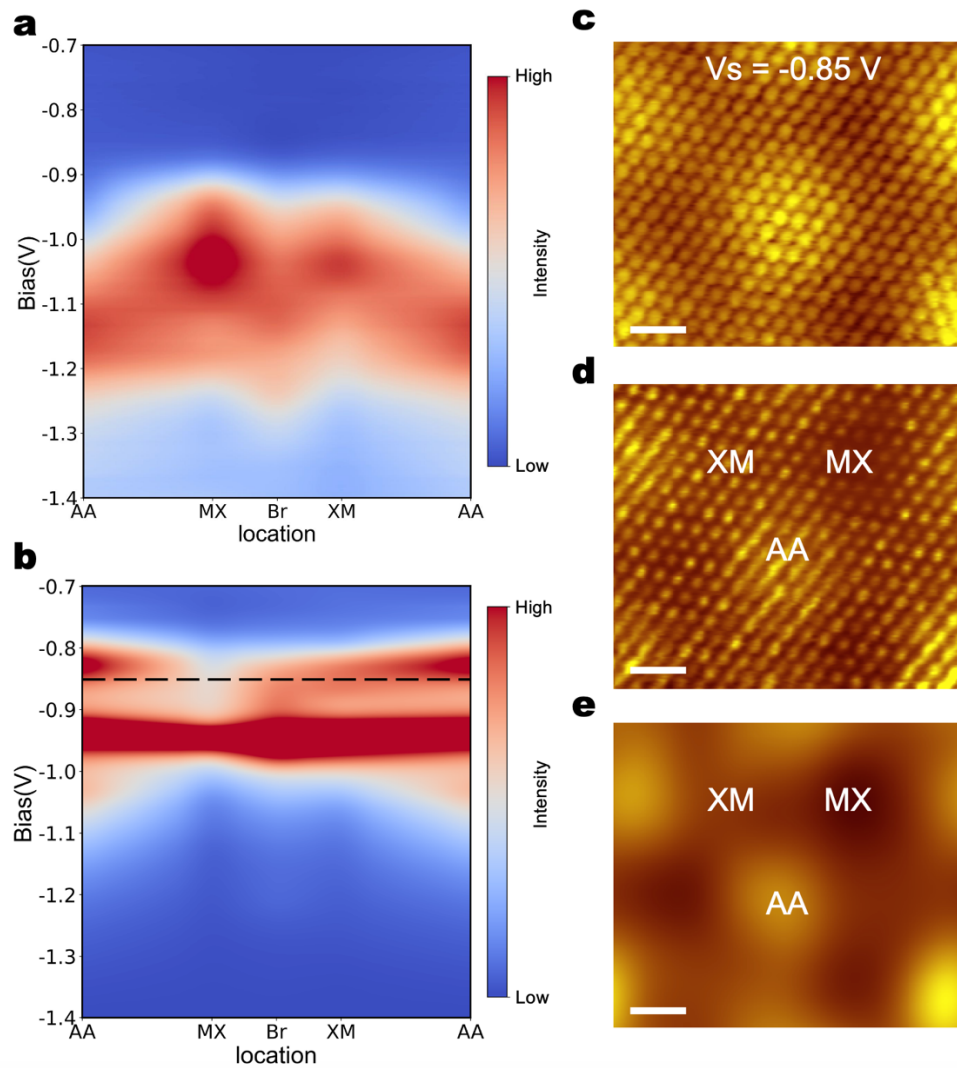


Figure 3 | Real space mapping of layer pseudospin. **a**, Constant-height and **b**, constant current STS color map along AA-MX-Br-XM-AA. **c-e**, topography (**c**), constant height dI/dV (**d**), and filtered dI/dV mapping images (**e**) at $V_s = -0.85$ V, the voltage highlighted by the dashed line in **b**. Scale bar: 1nm. ($V_s = -0.85$ V, $I = -40$ pA, $V_{amp} = 20$ mV)

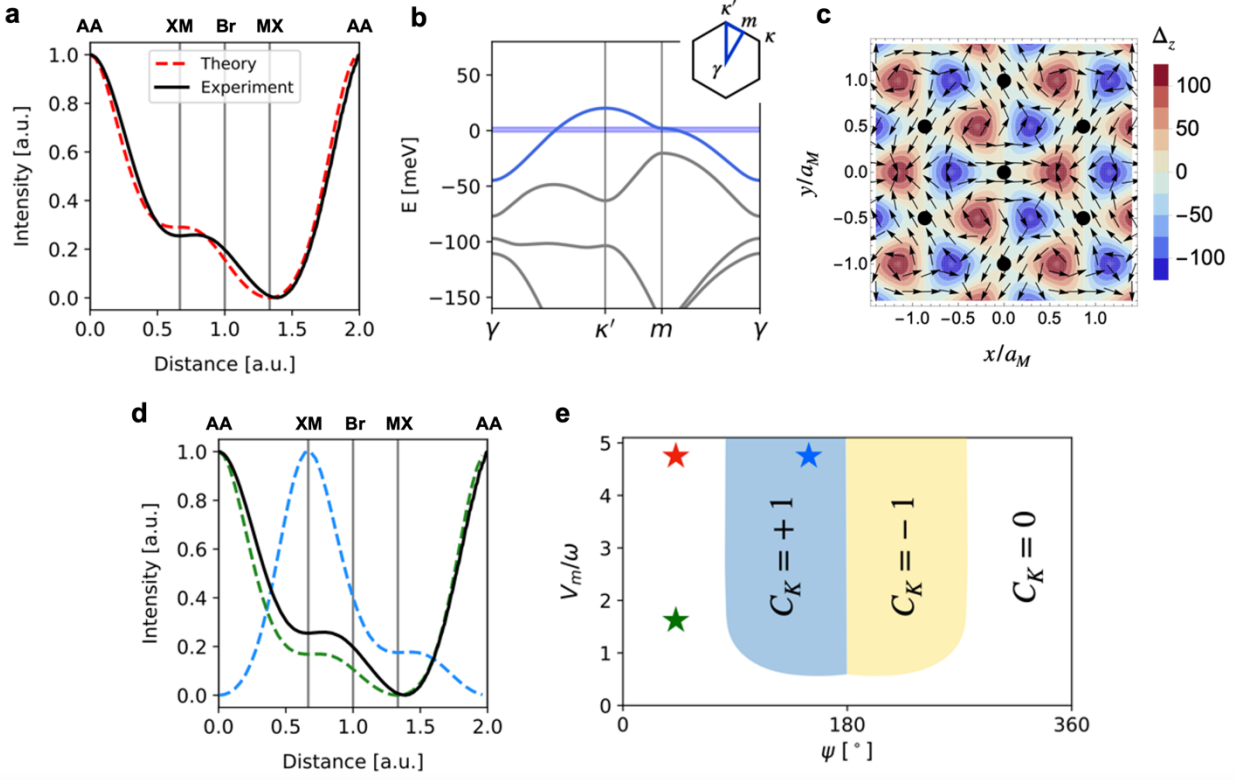


Figure 4 | Obtaining continuum model parameters from STS. **a**, Fit of the position-dependence of the layer-weighted LDOS near K_{VBM} . The black solid and red dashed lines are respectively experiment and theoretical fit. **b**, Moiré band-structure calculated with parameters obtained by fitting conductivity profile data along the high symmetry direction in Fig. 3e. The faint blue energy window marked where the theoretical LDOS curve in a is obtained. **c**, Layer-field Δ with arrows corresponding to the x and y components and color-scale corresponding the z component. Black dots indicate moiré superlattice AA sites. **d**, Position-dependence of the layer-weighted LDOS near K_{VBM} calculated with different set of parameters. Green curve: $V_m = 34.8$ meV, $\psi = 42.1$ degrees and $\omega = 21.6$ meV; Blue curve: $V_m = 34.8$ meV, $\psi = 150$ degrees and $\omega = 7.2$ meV. **e**, Chern number of the topmost moiré band from the continuum model as a function of ψ and V_m/ω at $\theta=5.08^\circ$. The $C_K=\pm 1$ regions are color coded. The red star labels the fitting showing in a. The green star and blue star respectively correspond to green curve and blue curve in Fig. 4d in the continuum parameter space.